

# Efficiency Measurement and Modeling of a High-Performance $\text{Mg}_2(\text{Si},\text{Sn})$ -Based Thermoelectric Generator

Julia Camut,\* Pawel Ziolkowski, Prasanna Ponnusamy, Christian Stiewe, Eckhard Mueller, and Johannes de Boor\*

$\text{Mg}_2(\text{Si},\text{Sn})$  is an attractive material class due to its excellent thermoelectric (TE) properties, its eco-friendly constituents, its low mass density, and its low price. A lot of research has been done on optimizing its TE properties; however, works on its use in thermoelectric generators (TEG) are scarce. Herein, the first conversion efficiency measurement of a functional, fully  $\text{Mg}_2(\text{Si},\text{Sn})$ -based TEG, approaching a maximum value of 4% for an applied  $\Delta T = 375^\circ\text{C}$ , is shown. A maximum power density of  $0.9\text{ W cm}^{-2}$  (related to the cross-sectional area of the TE legs) at  $\Delta T = 375^\circ\text{C}$  is also reported, which is among the highest performance of silicide-based modules reported in literature. Efficiency measurements can be tricky due to the uncertainty of heat flow measurement and parasitic heat losses; therefore, assessing the measurement reliability by confronting it to theoretical calculations is necessary. TEG device simulation in a constant property model is used to compare measured data to expected values and a good match is found (<1% deviation for current at maximum power, <4% difference for maximum power output, deviation within measurement uncertainty range for heat flows and efficiency). The significant discrepancy between measurement and calculations of the inner electrical resistance reveals room for improvement. Cracks form due to thermally induced mechanical stress, which dramatically increase the inner electrical resistance. It is shown that by avoiding those cracks, the maximum power output and conversion efficiency of the TEG could be improved by 30%.

## 1. Introduction

In the context of the increasing need for green sources of electrical energy, thermoelectric (TE) materials have gained a lot of interest over the past decades.<sup>[1]</sup> Their ability to convert heat flow into electrical power makes them highly attractive as, globally, about 60% of the primary energy is lost as waste heat.<sup>[2]</sup> Although their efficiency is not as high as other green energy sources, TE devices have the advantages of being reliable and needing no maintenance due to their lack of moving parts. This has made them an interesting energy source in various fields such as the aerospace industry, where radioisotope thermoelectric generators (RTGs) convert the heat released by the natural decay of radioactive materials into electricity supply of space missions.<sup>[3]</sup> Exhaust heat conversion to electricity in the automotive and in industrial processes is also among the most popular application.<sup>[3–5]</sup> On a smaller scale, thermoelectric technology is also considered to power wearable medical devices,<sup>[6–8]</sup> mobile storage of pharmaceuticals, and electronic devices.<sup>[3]</sup>


A thermoelectric generator (TEG) is a device in which semi-conducting n- and p-type TE elements, called legs, are connected electrically in series and thermally in parallel. Over the last decades, a large majority of the research in thermoelectrics has been focused on the optimization of the TE properties of various material classes as the first, very challenging step in the development chain of a TEG.<sup>[9–18]</sup> As a consequence, many material systems have not reached the TEG development stage yet and research on contacting techniques and on TE module building remained relatively scarce.<sup>[19]</sup>

Commercial TEGs based on  $\text{Bi}_2\text{Te}_3$ , the most mature material, are reported to reach an efficiency of 7.2% between room temperature and  $250^\circ\text{C}$  in continuous use.<sup>[20]</sup> However, the temperature range of stable  $\text{Bi}_2\text{Te}_3$  operation is bound to this upper limit, whereas the largest fraction of available waste heat is lost above,<sup>[21]</sup> which is why research focuses on materials and TEG operating at higher temperatures. High-performance modules using various materials were reported, such as half-Heusler compounds (8.3% efficiency and  $2.11\text{ W cm}^{-2}$  power density when operating between 342 and  $997\text{ K}$ <sup>[22]</sup>), Skutterudites (10.2% efficiency and  $1.6\text{ W cm}^{-2}$  power density between 298 and  $872\text{ K}$ <sup>[23]</sup>),

J. Camut, P. Ziolkowski, P. Ponnusamy, C. Stiewe, E. Mueller, J. de Boor  
Institute of Materials Research  
Department of Thermoelectric Materials and Systems  
German Aerospace Center  
51147 Cologne, North Rhein-Westphalia, Germany  
E-mail: julia.camut@dlr.de; johannes.deboor@dlr.de

E. Mueller  
Institute of Inorganic and Analytical Chemistry  
JLU Giessen  
35390 Giessen, Hessen, Germany

J. de Boor  
Faculty of Engineering, Institute of Technology for Nanostructures (NST)  
University of Duisburg-Essen  
47057 Duisburg, Germany

 The ORCID identification number(s) for the author(s) of this article can be found under <https://doi.org/10.1002/adem.202200776>.

© 2022 The Authors. Advanced Engineering Materials published by Wiley-VCH GmbH. This is an open access article under the terms of the Creative Commons Attribution License, which permits use, distribution and reproduction in any medium, provided the original work is properly cited.

DOI: 10.1002/adem.202200776

and PbTe (9% efficiency and  $3.6 \text{ W cm}^{-2}$  power density between 283 and  $873 \text{ K}$ <sup>[24]</sup>). PbTe/TAGS-based TEGs with up to 12% efficiency are also commercially available for temperatures between 200 and  $600 \text{ }^\circ\text{C}$ . However, the main disadvantage of those high-performance TE materials is that they are made of toxic and/or rare and expensive compounds, while their stability under test is quite low.<sup>[25]</sup> Their toxicity and scarcity make them unsuitable for mass applications, which hinders the breakthrough of TE technology beyond space and cooling applications.

In this study, the solid-solution  $\text{Mg}_2\text{Si}_{0.3}\text{Sn}_{0.7}$  was chosen as the chemical composition for both p- and n-type materials of the TEG. The n-type material exhibits a high reproducible figure of merit of up to  $zT = 1.4$ .<sup>[26]</sup> The figure of merit is the main parameter indicating a TE material's performance; it is defined as  $zT = \frac{\alpha^2 \sigma}{\kappa} T$  where  $\alpha$  is the Seebeck coefficient,  $\sigma$  the electrical conductivity, and  $\kappa$  the thermal conductivity. This value is among the best TE performance values in the mid-to-high temperature range, compared with other materials in a similar temperature range.<sup>[14,27]</sup> P-type  $\text{Mg}_2\text{Si}_{1-x}\text{Sn}_x$  has seen significant improvement over the last years with maximum  $zT$  rising from  $<0.1$  before 2010<sup>[28]</sup> to  $0.6$ ,<sup>[13]</sup> approaching that of other material classes that might or have been used together in a TEG with n-type  $\text{Mg}_2\text{Si}_{1-x}\text{Sn}_x$ , such as higher-manganese silicides (HMS), ZnSb, and  $\text{CeFe}_4\text{Sb}_{12}$ .<sup>[18,29,30]</sup> p-type  $\text{Mg}_2\text{Si}_{1-x}\text{Sn}_x$  was also chosen due to the advantages of using similar materials for both n- and p-type legs, which are explained below. This material system also has the important advantage of not being composed of toxic nor rare elements, unlike other materials presented above. It is also lightweight, which is advantageous for mobile applications, in particular for cars and aerospace.

Following the optimization of the TE properties, the next step toward TEG device development is applying a suitable electrode. The electrode, also referred to as metallization, is a metallic layer applied between the TE leg and the bridge. It can act as a diffusion barrier,<sup>[31]</sup> mechanical buffer, and/or as an agent to facilitate soldering/joining the leg to the bridge. Aluminum was previously shown to be a compatible electrode for p- and n-type  $\text{Mg}_2(\text{Si},\text{Sn})$ ,<sup>[32,33]</sup> and it was therefore used in this work as metallization layer. Using chemically similar p- and n-type materials can improve the mechanical stability of the module, even more if the same electrode is used for all legs, as the differential thermal expansion will be similar for all legs.<sup>[34]</sup> Some stress due to the remaining coefficient of thermal expansion (CTE) mismatch cannot be avoided; therefore, having the same material combination for all legs can also allow to find means to relieve this stress more easily.

Although silicides have been extensively studied in the field of TE properties optimization, not much work has yet been reported on the technological aspect of using them to build modules. Different studies have investigated  $\text{Mg}_2\text{Si}$ -based n-type unileg TEG, with limited performance.<sup>[35–38]</sup>  $\text{Mg}_2\text{Si}$  was also paired with Si–Ge, which gave a power density of  $1.8 \text{ W cm}^{-2}$  (with respect to the area of the TE legs) for  $T_h = 650 \text{ }^\circ\text{C}$  and  $T_c = 30 \text{ }^\circ\text{C}$ .<sup>[39]</sup>

Some studies also focused on the  $\text{Mg}_2(\text{Si},\text{Sn})/\text{HMS}$  combination for TEG.<sup>[29,40–42]</sup> Skomedal et al. reported a maximum power density of  $3 \text{ W cm}^{-2}$  (TE area) and predicted an efficiency of 5.3% for a possibly unrealistic  $T_h = 735 \text{ }^\circ\text{C}$ <sup>[41]</sup> with  $\text{Mg}_2(\text{Si},\text{Sn})$  as n-type. In a TEG cascaded with BiTe,<sup>[42]</sup> the  $\text{Mg}_2\text{Si}/\text{HMS}$  module alone reached a maximum efficiency of 8.5%, for  $T_h = 550 \text{ }^\circ\text{C}$  and  $T_c = 30 \text{ }^\circ\text{C}$ . Finally, a segmented TEG made of BiTe

and  $\text{Mg}_2\text{Si}/\text{HMS}$  gave a maximum power density  $0.8 \text{ W cm}^{-2}$  (TE area) for  $\Delta T = 498 \text{ K}$  and an efficiency up to 5% for  $\Delta T = 500 \text{ }^\circ\text{C}$  and  $T_c = 25 \text{ }^\circ\text{C}$ .<sup>[29]</sup>

Two fully  $\text{Mg}_2(\text{Si},\text{Sn})$ -based TEGs were reported previously. Gao's thesis reported a first attempt showing a maximum power output of  $117 \text{ mW}$  for  $T_h = 440 \text{ }^\circ\text{C}$  and  $T_c = 110 \text{ }^\circ\text{C}$ .<sup>[43]</sup> More recently, Goyal et al. reported a power density of  $0.52 \text{ W cm}^{-2}$  (TE area) and calculated a predicted maximum efficiency of 5%.<sup>[44]</sup> However, no measured efficiency was reported for such a TEG so far.

Measuring the heat flow (and with it the conversion efficiency) for small TEG prototypes is difficult due to the small heat flow it requires, as this amplifies, for geometrical reasons, the uncertainty related to thermal bypass. In this work, we present the first full characterization of a fully  $\text{Mg}_2(\text{Si},\text{Sn})$ -based TEG, including its conversion efficiency measurement. The reliability of the measurement is tested through comparison with calculations using the constant property model (CPM), which has the advantages of being simple but often precise enough, given the considerable experimental uncertainties.<sup>[45]</sup> Open-circuit voltage, inner electrical resistance, heat flow for open circuit and maximum power conditions, current for maximum power, maximum power output and maximum conversion efficiency are calculated and compared. Satisfying match is found for most parameters except the inner electrical resistance, which indicates some defects in the TEG and allows to identify room for improvement. The calculations are also used to analyze the cycling behavior of the TEG (over two measuring cycles) to understand changes at material and device level. Estimations of performance for improved contact qualities are provided for a technologically realistic range of achievable inner resistance of the TEG.

## 2. Experimental Section

### 2.1. Experimental

#### 2.1.1. Legs Preparation

Pellets of  $\text{Mg}_2(\text{Si},\text{Sn})$  solid solutions were prepared similarly to what were reported in previously published papers, with the following nominal stoichiometry:  $\text{Mg}_{2.06}\text{Si}_{0.3}\text{Sn}_{0.665}\text{Bi}_{0.035}$  for n-type (including excess Mg to compensate for Mg evaporation) and  $\text{Mg}_{1.98}\text{Li}_{0.03}\text{Si}_{0.3}\text{Sn}_{0.7}$  for p-type.<sup>[26,46,47]</sup>

The electrodes consisted of Al foil (Alfa Aesar, 99.99% purity) directly in contact with the TE pellet and a Cu foil (ChemPUR, 99.995% purity) on the outside of the pellets such as that shown in **Figure 1**. The Al foil is Ar etched and coated on both sides with a  $\approx 8 \mu\text{m}$  Zn layer, as it was previously shown that it was necessary to protect the Al surface with an oxidation barrier coating after etching to have high-quality electrical contacts.<sup>[33]</sup> The Ar-ion etching, Zn coating, and contacting process were similar to what was reported in this previous work.

After contacting, the pellets were diced into legs using a Disco DAD321 Automatic Dicing Saw. The cutting speed through the sample was  $0.3 \text{ mm s}^{-1}$  with an angular speed of 30 000 blade rotations per minute and each cut was made in a single pass. The whole process is summed up in **Figure 1**.

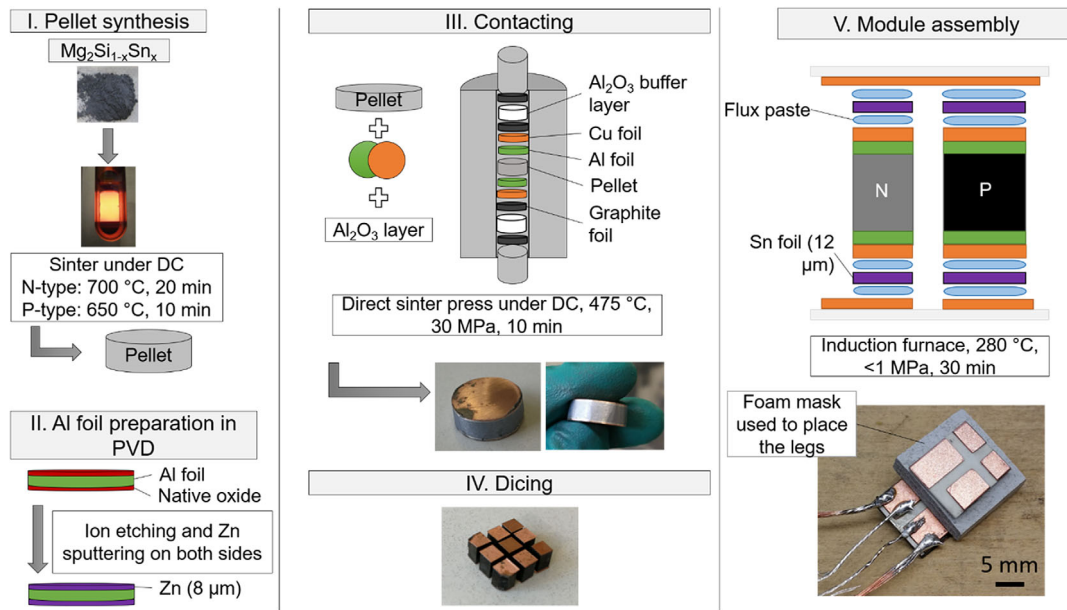


**Figure 1.** Preparation process from pellet fabrication over metallized legs to the thermoelectric module lab prototype. The foam mask used as leg spacer is made of Porotherm delivered by TECHNO-PHYSIK Engineering GmbH, Essen, Germany.

The quality of the joining between the metallization and the TE legs was gauged by the value of its specific contact resistance  $r_c$ , which could be measured using a potential and Seebeck scanning microprobe (PSM).<sup>[48,49]</sup> Two  $r_c$  values were obtained for each contact with two different calculation methods, using the TE material's known electrical conductivity to calculate the current density ( $r_{c,j(\text{TE})}$ ) or using the current passing through the sample as measured on a shunt resistor by the PSM ( $r_{c,j(\text{PSM})}$ ), as reported in previously published papers.<sup>[32,46]</sup> The two specific electrical contact resistances were calculated using the following equations.

$$r_{c,j(\text{TE})} = \frac{(V_{\text{elec}} - V_{\text{TE}}) * L}{\Delta V_{\text{TE}} * \sigma_{\text{TE}}} \quad (1)$$

$$r_{c,j(\text{PSM})} = \frac{(V_{\text{elec}} - V_{\text{TE}}) * A}{I_{\text{PSM}}} \quad (2)$$

Here,  $V_{\text{elec}} - V_{\text{TE}}$  is the drop in electrical potential at the interface between the electrode and the TE material and the position of interface being localized using the drop in Seebeck coefficient on the line scan.  $L$  is the length of the TE material (between the two electrodes),  $\Delta V_{\text{TE}}$  is the drop of potential along the TE material and  $\sigma_{\text{TE}}$  is the electrical conductivity of the TE material,  $A$  is the leg cross-section, and  $I_{\text{PSM}}$  the current measured in the device.

Evaluation of contact resistivities was conducted for the electrodes on each side of every leg. The  $r_c$  values obtained for the legs used to build the module studied in this work are reported in **Table 1**.

It can be seen that the electrical contact resistivities from both evaluation methods lie close to each other and within the limits of individual statistical distributions. Furthermore, contact resistivities are symmetric and low ( $<10 \mu\Omega \text{ cm}^2$ ), meaning that the

**Table 1.** Specific contact resistances (mean value  $\pm$  standard deviation) of the legs used to build the module. Each interface of each leg is reported to check for symmetry.

Leg	n-type		p-type	
	Side 1	Side 2	Side 1	Side 2
$r_{c,j(\text{TE})} [\mu\Omega \text{ cm}^2]$	$3 \pm 2$	$2 \pm 1$	$6 \pm 2$	$5 \pm 2$
$r_{c,j(\text{PSM})} [\mu\Omega \text{ cm}^2]$	$6 \pm 4$	$4 \pm 2$	$5 \pm 2$	$5 \pm 1$

contact between the TE material and the metallization should not impede the performance of the module.<sup>[50]</sup> For the following calculations, an average value of  $5 \mu\Omega \text{ cm}^2$  was considered for each TE/Al interface. The  $r_c$  value is also considered to be constant with temperatures, as the temperature dependence of the contact resistance between Ni electrodes and  $\text{Mg}_2\text{Si}$  was previously shown to be weak.<sup>[51]</sup> Therefore, the same value applies to both hot and cold sides of the TEG for following calculations.

**Table 2.** Details of the legs used for the module fabrication.

	n-type	p-type
Effective composition	$\text{Mg}_{2.0}\text{Si}_{0.3}\text{Sn}_{0.665}$ $\text{Bi}_{0.035}$	$\text{Mg}_{1.97}\text{Li}_{0.03}$ $\text{Si}_{0.3}\text{Sn}_{0.7}$
Cross section [mm $\times$ mm]	$3.4 \times 3.4$	$4.5 \times 4.5$
TE length before contacting [mm]	4.05	3.96
Total leg length (including electrodes) [mm]	4.30	

### 2.1.2. Module Fabrication

The details of the legs used for the fabrication of the module are reported in **Table 2**.

The module consisted of two unicouples and was assembled and joined in an induction furnace. The top and bottom substrates were standard commercial direct-bonded copper (DBC) plates obtained from HHI Industrievertretungen. The legs were soldered to the DBC using Sn foil (12.5 μm) as a solder. Flux paste was applied to both sides of the solder foil, as shown in Figure 1. The joining parameters were 280 °C for 30 min with a heating rate of 25 °C min<sup>-1</sup> and a load of 4 kg (0.6 MPa) under partial Ar atmosphere. The module had a filling factor of 31%, with respect to the area of the top DBC plate (top DBC: 15 × 13 mm<sup>2</sup>; bottom DBC: 14 × 25 mm<sup>2</sup>).

### 2.1.3. Module Testing

After assembly, the module performance was measured using an in-house built thermoelectric generator measurement apparatus (TEGMA) reported in other studies.<sup>[52–54]</sup> The measuring section of the setup was made of a heater, a geometry adaptor (copper), which distributed the heat flow on the hot side of the TEG over an appropriate cross section, the measured TEG, a nickel block (nickel LC992) that was used as a heat flow meter (HFM), and a cooling plate as a heat sink at the bottom of the configuration. To ensure good heat transfer between all components of the measuring section, graphite foils (Dr. Fritsch Gerätebau GmbH, 200 μm thickness) were inserted at all interfaces. The cold side temperature at the TEG was kept constant at 25 °C, while the hot side temperature was varied within the range from 200 to 400 °C. These values corresponded to interface temperatures of the coupling zones of the TEG, which were determined from an extrapolation of temperature profiles of the components adjacent to the TEG inside the measuring section.<sup>[38]</sup> Consequently, cold and hot side temperatures was not equal to effective temperatures at the TE legs but included temperature drops across graphite foils and DBC substrates. A schematic of the different temperatures along the measurement column is shown in the Supporting Information (Figure S2). The axial pressure applied to the TEG was about 3.9 MPa. The measurement was done under vacuum to eliminate convective heat losses, which could interfere with the heat flow measurement.

Measurement uncertainties of the TEGMA were determined for larger prototype and commercial TEG having significantly different properties compared with the module studied in this work. The uncertainty of open-circuit voltage was found to be 0.06% (for a measured value of 7.2 V)<sup>[53]</sup> (Supporting Information); the inner resistance had an uncertainty of 2.28% (for a measured value of 0.74 Ω)<sup>[53]</sup>; the heat flow had an uncertainty of 12% for a measured value of 100 W<sup>[52]</sup>; the power output had an uncertainty of 1.25% for a measured value of 2.5 W and the efficiency an uncertainty of 15.7% for a measured value of 4%.<sup>[55]</sup> Besides the choice of TE materials and contacting schemes, these deviations relate to the number of installed TE legs, their geometries, and the filling factor. Therefore, comparability to our TEG prototype is limited.

## 3. Theory and Evaluation

In order to check for the reliability of the measurement and identify loss mechanisms that impair module performance, model calculations on TEG performance were made to compare simulation results to measurements of the module performance. For the sake of simplicity, the constant properties model (CPM) was used, which assumes temperature-independent (averaged) properties along the TE legs using a method detailed (Equation (3)). Hence, the CPM approach neglects minor effects on the operation characteristics of TEGs such as Thomson heat and asymmetric distribution of Joule heat to the hot and cold sides of the leg. Furthermore, symmetric electric and thermal contact resistance between hot and cold side as well as between p- and n-type legs and the absence of parasitic heat bypass by radiation or convection were assumed.<sup>[56]</sup>

### 3.1. TE Properties and Temperature Average

In the CPM, average properties are assumed for the TE legs. While spatial averaging of electrical and thermal resistivities is physically appropriate, it was shown by Ponnusamy et al. that temperature averaging is satisfyingly reliable for the Mg<sub>2</sub>X materials in terms of efficiency prediction (with an uncertainty <2%, which is much smaller than the measurement uncertainty).<sup>[45]</sup> This method determines an averaged property  $\bar{X}$  between  $T_c$  and  $T_h$  such as

$$\bar{X} = \frac{1}{\Delta T} \int_{T_c}^{T_h} X(T) dT \quad (3)$$

All TE properties ( $\alpha$ ,  $\rho$ , thermal resistivity  $\frac{1}{\kappa}$ ) used in the following and previous CPM equations refer to temperature averages calculated using Equation (3). In particular,  $\kappa$  is calculated as the reciprocal of the average thermal resistivity such as  $\bar{\kappa} = \left( \frac{1}{\Delta T} \int_{T_c}^{T_h} \frac{1}{\kappa(T)} dT \right)^{-1}$ .

The TE properties data used for the calculations are shown in **Figure 2**. This experimental data was obtained from samples synthesized using the melting route described in previous work. It is reproducible and in the range of state-of-the-art values.<sup>[13,26]</sup>

Due to the contacting procedure involving Zn, a slight gradient in the Seebeck coefficient appears in n-type legs spreading from the contact faces. An exemplary PSM linescan is shown in Supporting Information (Figure S1) and another example can be also seen in the study by Camut et al.<sup>[33]</sup> Given the limited magnitude of the change ( $\leq 11\%$ , locally), this should have only minor impact on the module properties.

### 3.2. Determining the Temperature Conditions at the TE Legs

In order to make precise calculations, the effective temperatures at the TE legs had to be determined, as there were parasitic temperature drops across the elements of the measurement column, as represented in Supporting Information (Figure S2), and only the temperatures at the interface between the TEG and the elements of the column are measured. The effective hot and cold side temperatures at the TE legs are defined by  $T_{h,TE}$  and  $T_{c,TE}$ ,

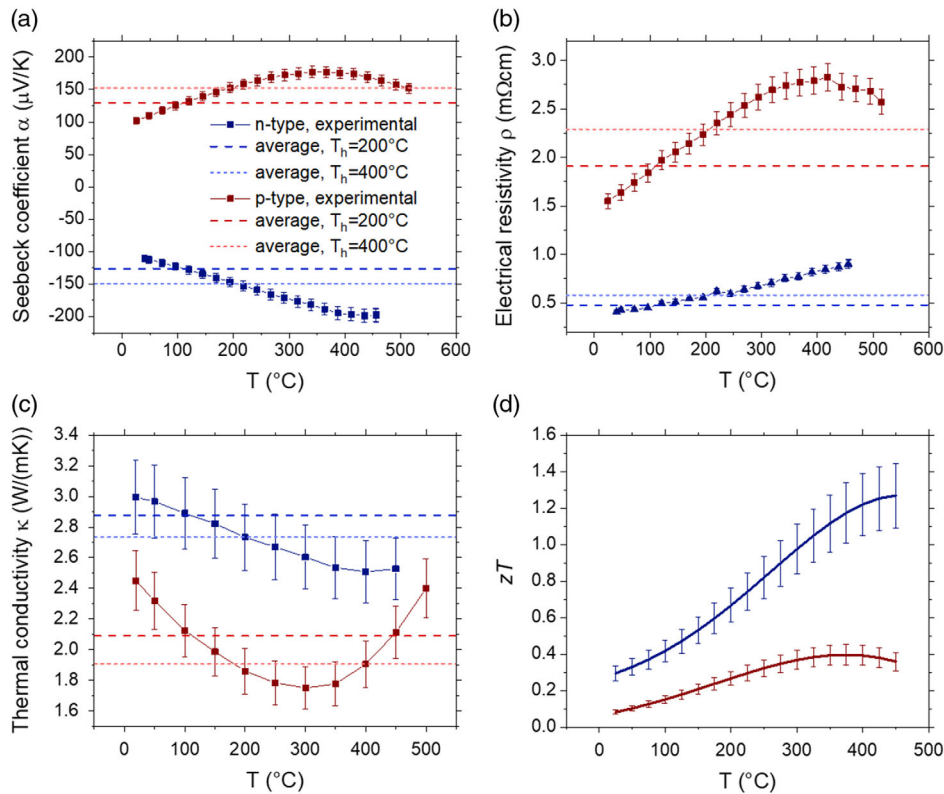


**Figure 2.** Measured properties of  $\text{Mg}_2\text{Si}_{0.3}\text{Sn}_{0.665}\text{Bi}_{0.035}$  (n-type) and  $\text{Mg}_{1.97}\text{Li}_{0.03}\text{Si}_{0.3}\text{Sn}_{0.7}$  (p-type) materials used as input for the CPM calculations: a) Seebeck coefficient, b) electrical resistivity, c) thermal conductivity, d) figure of merit. Uncertainties of the Seebeck coefficient and electrical conductivity measurement are 5% of the thermal conductivity 8%. The resulting uncertainty of  $zT$  is 14%. Exemplary temperature averages of each property for temperatures at the TE legs are given, for hot side temperatures of 200 and 400  $^{\circ}\text{C}$  and a cold side temperature of 25  $^{\circ}\text{C}$ . The legend in (a) also applies for (b), (c), and (d).

respectively, and we define the temperature difference at the TE legs such as  $\Delta T_{\text{TE}} = T_{\text{h,TE}} - T_{\text{c,TE}}$ .

The open-circuit voltage is the thermovoltage generated by the TEG due to the Seebeck effect by applying a temperature difference to the legs.<sup>[57]</sup> Using the measured open-circuit voltage  $U_{0,m}$ , the effective temperature difference at the TE legs at open loop  $\Delta T_{\text{TE},0} = \Delta T_{\text{TE}}(I = 0)$  can be obtained from the number of uncouples ( $N$ ) and their Seebeck coefficient averages ( $\alpha_n$ ,  $\alpha_p$ ) such as

$$\Delta T_{\text{TE},0} = \frac{U_{0,m}}{N(\alpha_p - \alpha_n)} \quad (4)$$

$n$  and  $p$  subscripts designate n-type and p-type materials (for all following equations as well). Then, the temperatures at the hot and cold side of the TE legs can be obtained assuming a symmetrical temperature loss across graphite foils and DBC substrates such as  $T_{\text{h,TE}} = T_{\text{h,m}} - 0.5 \times (\Delta T_{\text{m}} - \Delta T_{\text{TE}})$  and  $T_{\text{c,TE}} = T_{\text{c,m}} + 0.5 \times (\Delta T_{\text{m}} - \Delta T_{\text{TE}})$ , where  $T_{\text{c,m}}$  and  $T_{\text{h,m}}$  are the measured cold and hot side temperatures at the interfaces between the TEG and the heat flow meter and the heater, respectively.

When applying Equation (4), the Seebeck coefficient averages  $\alpha_p$ ,  $\alpha_n$  are calculated in a first iteration assuming  $T_{\text{h,TE}} \approx T_{\text{h,m}}$  and  $T_{\text{c,TE}} \approx T_{\text{c,m}}$ , which leads to some error in the obtained

$\Delta T_{\text{TE}}$ ,  $T_{\text{c,TE}}$ , and  $T_{\text{h,TE}}$ . However, Equation (4) was reapplied in a second iteration with new  $\alpha_p$ ,  $\alpha_n$  average values corresponding to the temperature conditions at the TE legs obtained in the first iteration. The obtained temperatures converge in only two iterations due to the weak slope of  $\alpha(T)$ .

An obvious error in this method arises from the assumed symmetrical distribution of the parasitic temperature drop between hot and cold sides to obtain values of  $T_{\text{c,TE}}$  and  $T_{\text{h,TE}}$ . In reality, the distribution is likely not symmetrical as there is a temperature dependence of the thermal contact resistance between each layer as well as of the thermal resistance of the graphite and ceramic plates. Calculations with other heat loss distributions are shown in Supporting Information (see Figure S5) and it will be shown in this paper that good match is still found with the symmetry assumption.

Other methods shown in the Supporting Information can be used for determination of the effective temperature conditions at the TE legs using the measured heat flow. However, as the measurement uncertainty of the heat flow is larger, especially at higher temperatures, we find them to be less reliable.

### 3.3. Temperatures at the TE Legs for $I \neq 0$

The temperatures at the TE legs obtained as described above only apply in case of open-loop conditions. However, due to the

influence of the Peltier heat, the temperature difference at the TE legs decreases when current is flowing and most TEG parameters are relevant for  $I \neq 0$ .

The parasitic temperature drop at the coupling zones between the TE legs and the HFH/heater,  $\Delta T_{\text{par,h}}$  and  $\Delta T_{\text{par,c}}$  respectively, are represented in Supporting Information (Figure S2). Considering  $\Delta T_{\text{par}} = \Delta T_{\text{par,c}} + \Delta T_{\text{par,h}}$ , we define  $\Delta T_{\text{par},0} = \Delta T_{\text{par}}(I = 0)$  and  $\Delta T_{\text{par,opt}} = \Delta T_{\text{par}}(I = I_{\text{opt}})$ , where  $I_{\text{opt}}$  is the current at maximum power output. Assuming that the thermal resistance of the parasitic layers does not vary with current,  $\Delta T_{\text{par}}$  varies proportionally to the heat flow only, therefore

$$\frac{Q_{\text{opt,m}}}{Q_{0,m}} = \frac{\Delta T_{\text{par,opt}}}{\Delta T_{\text{par},0}} = \frac{\Delta T_{\text{m,opt}} - \Delta T_{\text{TE,opt}}}{\Delta T_{\text{par},0}} \quad (5)$$

where  $Q$  is the measured incident heat flow and “0” and “opt” subscripts respectively refer to parameters at open-loop conditions and at optimum current for maximum power.  $\Delta T_{\text{par},0}$  is known such as  $\Delta T_{\text{par},0} = \Delta T_{\text{m},0} - \Delta T_{\text{TE},0}$ . From Equation (5),  $\Delta T_{\text{TE,opt}}$  is calculated and the corresponding hot and cold side temperatures,  $T_{\text{h,TE,opt}}$  and  $T_{\text{c,TE,opt}}$ , can be determined assuming symmetric losses.

Incident heat flows are not directly measured by the used configuration of the TEGMA, since a heat flow meter has been used at the cold side of the TEG only. Thus,  $Q_{\text{m}}$  is obtained by adding the measured values of the heat flow exiting at the cold side of the TEG ( $Q_{\text{out,m}}$ ) to the power output ( $P_{\text{m}}$ ) at a given current, such as  $Q_{\text{m}} = Q_{\text{out,m}} + P_{\text{m}}$ .

### 3.4. Heat Flows

Within CPM the heat flow at maximum power  $Q_{\text{opt}}$  is calculated using the following equations.

$$Q_{\text{opt}} = K_{\text{TE}} \Delta T_{\text{TE,opt}} + I \cdot N \cdot (\alpha_{\text{p}} - \alpha_{\text{n}}) T_{\text{h,TE,opt}} - \frac{1}{2} I^2 R \quad (6)$$

$$I_{\text{opt}} = \frac{N(\alpha_{\text{p}} - \alpha_{\text{n}}) \Delta T_{\text{TE,opt}}}{2R} \quad (7)$$

where  $R$  is the inner electrical resistance and  $K_{\text{TE}}$  the thermal conductance of the TE legs such as

$$R = R_{\text{TE}} + R_{\text{c}} = N \left[ \frac{\rho_{\text{p}} L}{A_{\text{p}}} + \frac{\rho_{\text{n}} L}{A_{\text{n}}} + 2r_{\text{c}} \left( \frac{1}{A_{\text{p}}} + \frac{1}{A_{\text{n}}} \right) \right] \quad (8)$$

$$K_{\text{TE}} = N \left( \frac{\kappa_{\text{p}} A_{\text{p}}}{L} + \frac{\kappa_{\text{n}} A_{\text{n}}}{L} \right) \quad (9)$$

where  $R_{\text{TE}}$  is the total electrical resistance of the TE legs and  $R_{\text{c}}$  the total electrical contact resistance. Equation (8) neglects the resistance of the metallic layers (Al metallization, Cu metallization, Cu bridges) and the contact resistances between them and  $R_{\text{c}}$  is assumed to mainly originate from the Al/TE interface.

For the open-loop heat flow,  $Q_0$ , Equation (6) is applied for  $I = 0$ , using  $\Delta T_{\text{TE},0}$  and  $T_{\text{h,TE}}(I = 0)$ , and  $K_{\text{TE}}$  is calculated for open-loop temperature conditions.

### 3.5. TEG Performance

For all following parameters, temperature conditions at maximum power are considered, even for maximum efficiency. Indeed, our measurement shows that there is between 1% and 2% difference between  $I_{\text{opt},\eta}$  (current at maximum efficiency) and  $I_{\text{opt}}$ ; therefore, the heat flow and temperatures at the TE legs will be similar for both current conditions (see Figure S6 in Supporting Information).

The performance of a TEG is mainly assessed by its power output and conversion efficiency. The maximum power output is generally given by<sup>[58]</sup>

$$P_{\text{max}} = N(P_{\text{n}} + P_{\text{p}}) = \frac{(N(\alpha_{\text{p}} - \alpha_{\text{n}}) \Delta T_{\text{TE,opt}})^2}{4R} \quad (10)$$

The maximum efficiency  $\eta_{\text{max}}$  of a TEG in the CPM can be obtained using the following equation.

$$\eta_{\text{max}} = \frac{T_{\text{h,TE,opt}} - T_{\text{c,TE,opt}}}{T_{\text{h,TE,opt}}} \frac{\sqrt{1 + ZT_{\text{m}}} - 1}{\frac{T_{\text{c,TE,opt}}}{T_{\text{h,TE,opt}}} + \sqrt{1 + ZT_{\text{m}}}} \quad (11)$$

where  $T_{\text{m}}$  is the average of  $T_{\text{c,TE,opt}}$  and  $T_{\text{h,TE,opt}}$ .  $ZT_{\text{m}}$  is the device figure of merit with

$$Z = \frac{N^2(\alpha_{\text{p}} - \alpha_{\text{n}})^2}{K_{\text{TE}} R} \quad (12)$$

In Equation (11) and (12), the temperatures at the TE legs are considered for more precision. In literature, the measured temperatures at the outside of the TEG are more commonly applied.

### 3.6. Inner Electrical Resistance

The inner electrical resistance of the TEG is calculated using Equation (8). Two leads are soldered to each TEG terminal in order to conduct a four-point measurement, which allows to neglect the resistance contributions of the current leads and potential probes. The detailed description of the procedure for measuring  $R$  is given in other studies.<sup>[39,40]</sup>

## 4. Results

Figure 3a shows the result of the two-cycles measurement for the open-circuit voltage. A significant increase of 12% is observed in the measured open-circuit voltage between the start and end of the first cycle, which is followed by an increase of up to 2% in the second cycle. This change will be compared to the change of other properties and commented.

The first-cycle cooling data is used for calculation of temperatures at the TE legs on the hot and cold side for  $I = 0$  and  $I_{\text{opt}}$ . If we calculate the ratio  $\Delta T_{\text{TE}}/\Delta T_{\text{m}}$ , it is found that respectively 5–11% (corresponding to 7 to 41 K) and 5–12% of the temperature difference is lost through the coupling, rising with increasing hot side temperature, as shown in Figure 3b.

Figure 3c–f shows the two-cycle measurement and calculations of other parameters: the inner resistance, heat flows (for open circuit and maximum power), and the current for

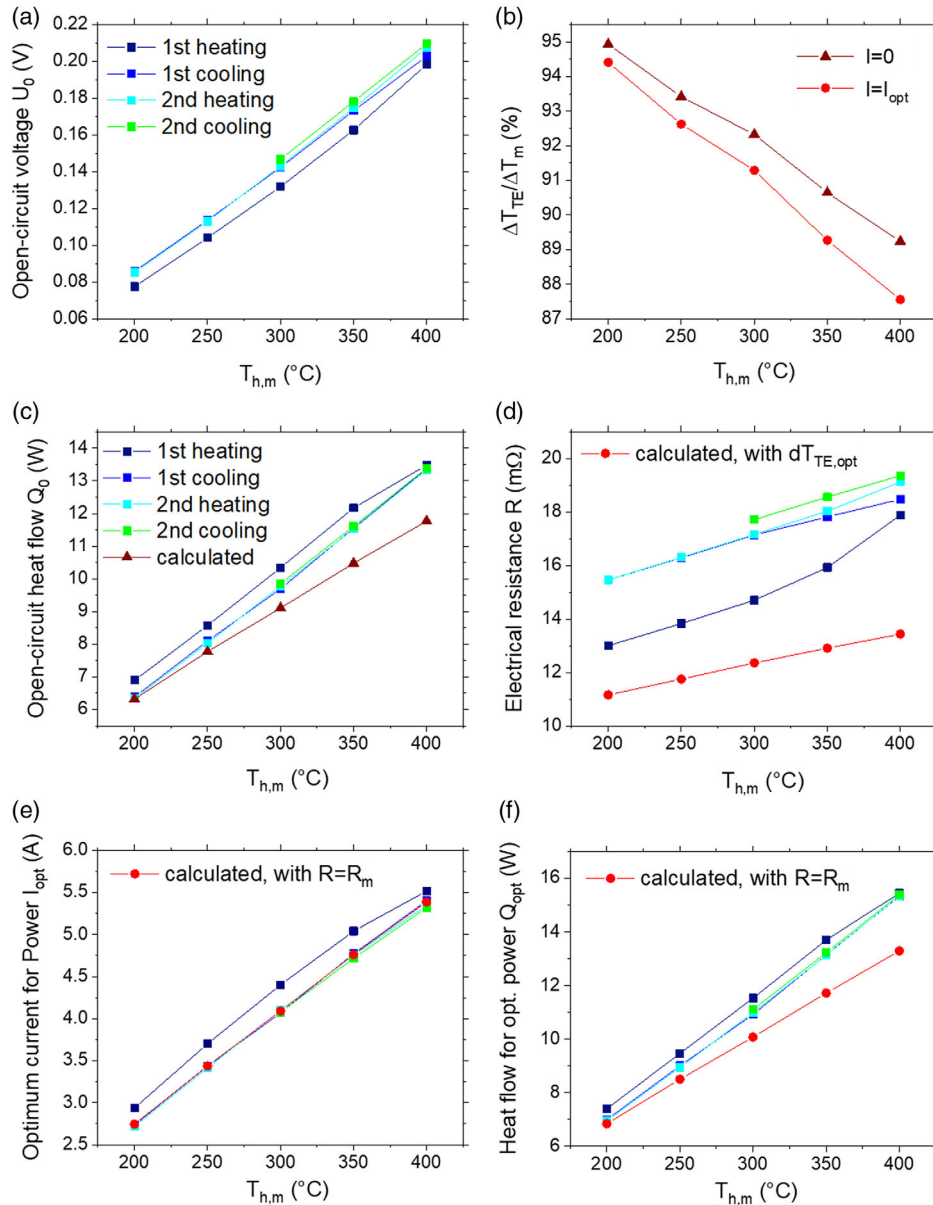


**Figure 3.** a) Two-cycles measurement of open-circuit voltage and b) ratio of the temperature differences at the TE legs and across the device for  $I = 0$  and  $I = I_{opt}$ . Two-cycles measurement and calculations of: c) heat flow at open circuit, d) inner electrical resistance, e) optimum current for maximum power, and f) heat flow at maximum power. The calculated data was obtained from the first cooling step.  $R_m$  is the measured electrical resistance. The legend of the measured data (blue to green hues, indicated in a)) also applies in (d), (e), and (f).

maximum power. It can be seen that a significant change occurs for all quantities during the first heating and cooling periods, followed by a more stable behavior in the next cycle, similar to what was observed for open-circuit voltage in Figure 3a. Changes during cycling can usually be attributed to three main factors: coupling quality (thermal transfer between TEG and TEGMA components), material change, and crack formation.

The decrease in heat flow (7% for  $Q_0$ ) could indicate that the coupling quality degraded during the first heating step. This is opposed to the observed increase in open-loop voltage, as a lesser thermal transfer would rather decrease  $\Delta T_{TE}$ . The increase in

open-circuit voltage despite a decrease of  $\Delta T_{TE}$  could be due to an increase of Seebeck coefficient. However, comparative line-scans of the Seebeck coefficient of an n-type and p-type leg are shown in Supporting Information (Figure S1). This magnitude of change (<7% for the n-type leg, <4% for the p-type) can alone explain only a minor fraction of the observed variation in the open-loop voltage. Similarly, the expected increase in material resistance is <10% (estimated using a single parabolic band model), way smaller than the observed increase, which therefore likely indicates the formation of cracks. If the cracks are located inside the TE legs (not at the interfaces with the metallization), it

would lead to an increase of  $\Delta T_{TE}$  and therefore the open-loop voltage, as we observe.

Figure 3d shows the comparison between calculated and measured values of the total inner resistance. At the start of the measurement, the difference between measurement and calculation was 15%; by the end of the first cooling step, it increased to 28%. The calculated data sums the resistance of the TE legs and the contact resistances using the specific resistivity reported in Table 2. The considered contact resistance represents 2% of the calculated total inner resistance. The far larger measured  $R$  indicates that there is additional resistance in the electrical circuit, which was not yet accounted for, and that it increases with cycling (large increase in the first cycle, smaller in the second). This could come from additional contact resistance (poor soldering, progressive delamination of metallization) or from crack formation, which would hinder the current flow.

The optimum current for maximum power shows a deviation <1% between measurement (first cooling) and calculation (using the measured  $R$ ). This slight deviation could come from the small change in n-type Seebeck coefficient.

The temperature profile in the cold side heat flow meter is shown in Figure S7 in the Supporting Information. It can be seen that there is a 5–12 K temperature difference, for a heater temperature of 200 °C and 400 °C respectively, which is sufficiently large for reliable estimation of the heat flow. The measured open-circuit heat flow (first cooling) is 1–14% higher than the calculated value with increasing hot side temperature, similar to the heat flow for optimum power, which shows a difference of 2–15%. This is in the range of measurement uncertainty reported in the study by Ziolkowski et al.,<sup>[52]</sup> except for the highest temperature for which the deviation is higher than the uncertainty threshold. This threshold was however determined for commercial-scale TEG (more legs, larger filling factor) and therefore does not necessarily apply to our prototype.

The similarity between observed differences for open-loop and nonzero current conditions indicates that the deviation between measurement and calculation does not highly depend on electric current flow and associated effects like Joule, Thomson, and Peltier heat and their asymmetry. Although there could be compensating effects, it gives a good hint that the CPM is applicable.

Said deviation would rather originate from discrepancies between true and supposed TE properties, temperature conditions, and of course from cracks and possible TEG-internal heat bypasses, not considered in the CPM. The increase of the difference with increasing temperature indicates that the deviation is likely due to the increase of the heat bypass inside the TEG by means of radiation.

Figure 4 shows the comparison of two-cycles measurement and calculations for maximum power output and efficiency. The increase of both open-circuit voltage and inner resistance compensates such that the maximum power remains relatively stable throughout cycling (<3.5% change between cycling steps). An increase in maximum efficiency is observed between the first heating and cooling, due to the corresponding decrease in heat flow.

The higher measured electrical resistance  $R_m$  will have an impact on the deviations of further calculations which depend on this parameter. Independently from the cause of this increased resistance (contacts or cracks), the increase can be considered analytically as “effective” contact resistance such as

$$r_{c,m} = \frac{(R_m - R_{legs})A_n}{2N\left(1 + \frac{A_n}{A_p}\right)} \quad (13)$$

The obtained values for  $r_{c,m}$  evolve from 85 to 99  $\mu\Omega \text{ cm}^2$  with increasing hot side temperature.

The power output and efficiency measurements give a maximum power of 0.55 W (density 0.9  $\text{W cm}^{-2}$  with respect to the total TE leg area) and a maximum efficiency of 3.6%. The calculations are made using both  $r_{c,m}$  and the initial  $r_c = 5 \mu\Omega \text{ cm}^2$  measured between the TE material and the metallization, before the TEG assembly. Therefore, the calculations using  $r_{c,m}$  represent the actual TEG while the calculations using  $r_c$  represent a realistic goal, without cracks and with the in-principle achievable low-contact resistances. The difference between measurement and  $r_{c,m}$  calculations is 2–4% for maximum power and 1–10% for maximum efficiency. The larger difference of the latter is due to the deviation between calculated and measured heat flow.

To trace the origin of the observed high electrical resistance, scanning electron microscopy (SEM) investigation was performed. However, as this implied to embed the TEG for

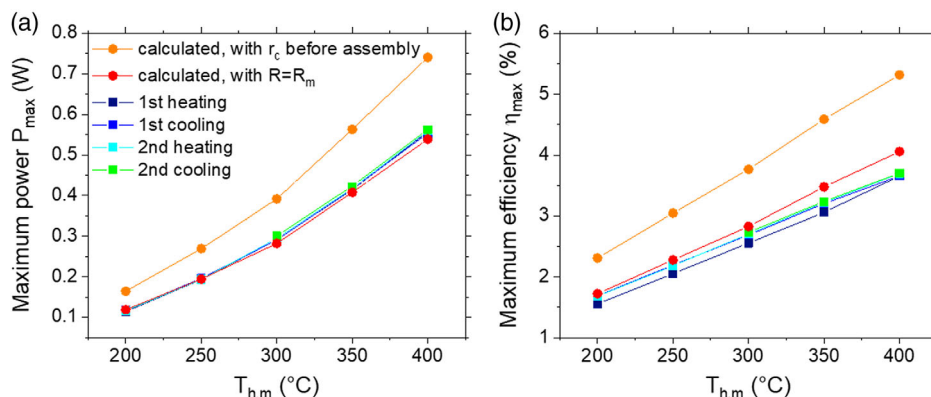


**Figure 4.** Comparison between measurement, calculations using contact resistance measured on the metallized legs before TEG assembly, and using contact resistance obtained from measured inner resistance, for: a) maximum power output and b) maximum efficiency. The legend in (a) also applies to (b).



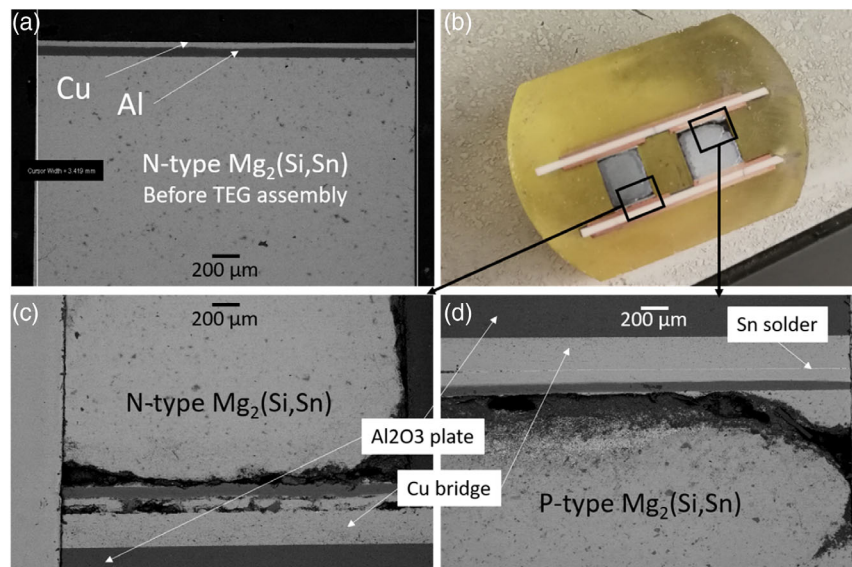


**Figure 5.** a) Representative SEM observation of a metallized leg before TEG assembly, b) photograph of a TEG unicouple made under identical conditions as the prototype measured and shown in Figure 3 and 4, c) SEM close-up of the junction between n-type leg and bridge indicated in (b), and (d) SEM close-up of the junction between p-type leg and bridge indicated in (b).

preparing a polished section, which would prevent any further characterization, we set up another unicouple prototype under identical conditions especially for SEM investigations; the results are shown in **Figure 5**. As this unicouple has been assembled with an identical procedure as the TEG discussed in this paper, it can give some hints on the state of the measured TEG, at least prior to its performance measurement. However, as TEG fabrication is a multistep process, there is of course some variability which limits the similarity of this unicouple analysis to the measured TEG.

It can be observed in **Figure 5a** that prior to assembly, no crack can be seen between the different components of the metallized leg. However, after the TEG assembly step (280 °C, 30 min, 0.6 MPa), cracks formed in the TE material next to the metallization layer. Such cracks are definitely a source of increased inner electrical resistance in a module, especially given that the hot side temperature during the measurement goes beyond 280 °C, so crack formation is even more likely. It is however supposed that the cracks in the measured TEG are not that wide as in the embedded TEG (possibly due to applied pressure in the measurement or due to a possible widening during the embedding process), as no current would flow through cracks like observed in **Figure 5**.

It can also be seen in **Figure 5c** that the Cu–Cu junction (between leg and bridge) looks suboptimal, while the other Cu–Cu interface shown in **Figure 5d** looks very clean. The visual quality of those contacts seems variable; it is therefore hard to conclude on the quality of the actual interfaces in the cycled TEG and on their impact on the electrical resistance.

## 5. Discussion

The TEG was measured for two cycles with a cold side temperature at 25 °C and a hot side temperature varying between 200 and

400 °C. After successfully assembling and characterizing the TEG, the reliability of the experimental data must be assessed by comparison to theoretical calculations. The CPM was chosen for its simplicity. The open-circuit voltage was used to determine the temperature conditions at the TE legs, which lead to low deviations between measurement and calculations for heat flows and current at maximum power. This indicates reliable efficiency and power measurement results, within the uncertainty budgets of the employed measurement techniques. This work reports the first efficiency measurement of a fully  $\text{Mg}_2(\text{Si,Sn})$ -based TEG.

**Figure 6** shows the performance of other TEG lab prototypes reported in literature for the low-to-mid-temperature range, especially silicide-based TEGs. It can be seen that Sb- and Te-based modules still have better performance; however, they are composed of materials which are more toxic and have a lower temperature application range.<sup>[59,60]</sup> The power output of our TEG is higher than the power reported for the only other fully  $\text{Mg}_2(\text{Si,Sn})$ -based TEG, due to a shorter and wider leg geometry (no measured efficiency reported).<sup>[44]</sup> Both its power output and efficiency are higher than the performance reported for a segmented TEG combining the high performance of silicides and BiTe.<sup>[29]</sup> Moreover, the performance of our TEG is similar to the  $\text{Mg}_2(\text{Si,Sn})/\text{HMS}$  TEG reported by Skomedal et al.<sup>[41]</sup> while offering a simpler design. It is also much higher than the performance of other green materials class such as oxides. Finally, room for (large) improvement, discussed later, is identified in our TEG and the expected performance would exceed most previously reported values of silicide modules.

In order to reach the predicted optimal performance (increase by 30%), the origin of the differences between predicted and measured performance needs to be identified. The reduced power mainly originates from the electrical resistance, for which there is large disagreement between the measurement and the CPM calculations. From SEM investigations on a similar

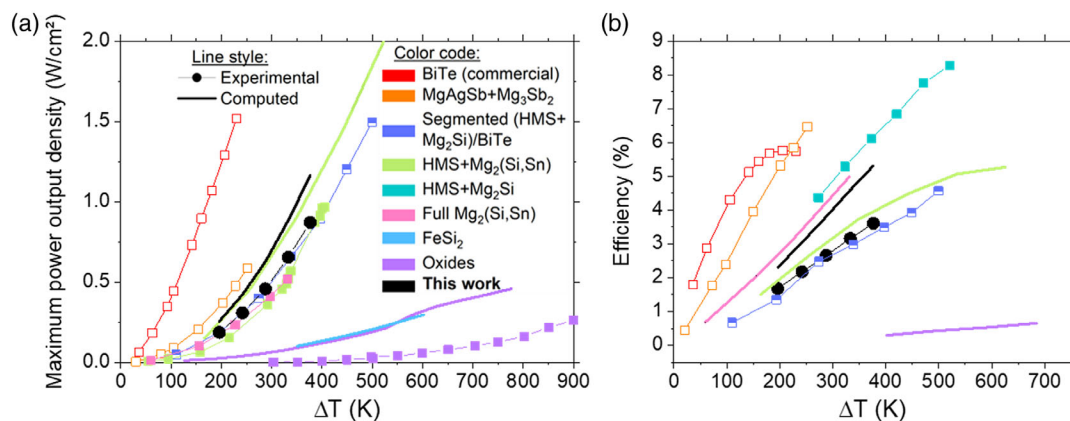


**Figure 6.** Performance of literature silicide-based and low-temperature TEGs: a) maximum power and b) efficiency. The legend indicated in (a) is magnified in c) for better readability and also applies to (b). Symbols + lines indicate measured data; simple lines indicate calculated data. Empty symbols indicate toxic compounds. Data were taken from other studies.<sup>[29,41,44,59–64]</sup>

unmeasured TEG, it is plausible that cracks were present close to one or several TE/Al interfaces before starting the module test measurement. This agrees with the fact that the resistance at the start of the measurement was already higher than expected. It is possible that the cracks expanded during the first heating step, which would increase the inner resistance. An increase is seen in the open-circuit voltage during the first heating step. Since the TE leg's properties are found to be relatively stable, this indicates that the temperature difference across the TE legs increased during this cycle. A corresponding increase in heat flow should be observed if this was due to better thermal transmission; however, the heat flow decreases during the first cycle, which could be explained by the widening of the cracks in the legs.

Cracks were already observed in Mg<sub>2</sub>(Si,Sn) legs composing TEGs. Mejri et al.<sup>[65]</sup> and Skomedal et al.<sup>[41]</sup> both reported crack formation on the hot side of the TEG after characterization. Kaibe et al.<sup>[42]</sup> provided finite elements methods analysis of their cascaded TEG (partially composed of Mg<sub>2</sub>(Si,Sn)) and confirmed that tensile stresses are localized at the interface of the hot side electrode of the silicide module, which is probably a major origin of the reported fatigue damage.

Given that the cracks are parallel to the interface, it is unlikely that they are due to a too high axial pressure, but it could rather be an indication of a mismatch in CTE, which has already been seen for other electrodes. The Al and Cu foils (CTE of 21–24 × 10<sup>-6</sup> and 17 × 10<sup>-6</sup> K<sup>-1</sup> respectively) of the metallization were contacted at 475 °C, which means that if there was a CTE mismatch between the TE material (CTE of Mg<sub>2</sub>(Si,Sn) about 16–18 × 10<sup>-6</sup> K<sup>-1</sup><sup>[65–67]</sup>) and those layers, the cracks should have already appeared in the metallized legs before TEG assembly (280 °C). Therefore, the thermal stress probably arises from Al<sub>2</sub>O<sub>3</sub> in the DBC plate (CTE 8 × 10<sup>-6</sup> K<sup>-1</sup>) and not from the metallic layers.

Such stress could be partially relieved using DBC plates only at the cold side, while using a more flexible design at the hot side (i.e., cut DBC plates or loose metallic bridges<sup>[68,69]</sup>). Besides changing the TEG design toward more flexible constructions and material choice with better accordance of CTE, other

parameters can be optimized to increase mechanical stability of the module. Two studies reported a reduced stress by changing the shape of the cross section of the TE legs,<sup>[70,71]</sup> and increasing leg length is also recommended,<sup>[72]</sup> although the latter will have a direct impact on the module's thermal resistance.

Nevertheless, the increase of open-loop voltage and inner resistance compensate such as the maximum power is stable during both cycles of the measurement. The efficiency, similar to the heat flow, settles after the first heating and keeps a stable value during the second cycle of the measurement. Considering the heat flow measurement, besides its larger specified measurement uncertainty (which is not directly applicable to our TEG due to its geometry), it is also possible that it was overestimated due to a thermal bypass. It is indeed likely that some heat is transmitted as radiation between the heater and the bottom part of the TEG or the HFM, given its small size. This heat would impact the heat flow measurement in the HFM and therefore the efficiency value. Such thermal bypass can be estimated by calculating the radiative heat flow  $Q_{rad}$  emitted by the Cu heater and received by the exposed surfaces of the bottom DBC and the top of the HFM. Following the procedure described in SI, it is found  $Q_{rad} \approx 0.3$  W at  $T_{h,m} = 400$  °C while the difference between expected and measured values of  $Q_0$  and  $Q_{opt}$  is  $\approx 2$  W. The real value of  $Q_{rad}$  is probably larger, considering that thermal bypass would also be absorbed by the lateral sides of the HFM, which would have an impact on the measured temperature profile, used to determine the heat flow. Such calculations are however quite complicated; therefore, a simple, quantitative estimate cannot be given. As a consequence, the measured efficiency is probably underestimated and the "real" value could actually rather be  $\approx 4.2\%$  at  $T_{h,m} = 400$  °C (dividing measured maximum power by expected heat flow at maximum power). To get more accurate values, the measurement setup could be optimized to better accommodate small device geometries and limit parallel parasitic heat flows, using heating and cooling elements of matching cross section compared with the TEG surface.

Finally, the use of the CPM calculations is found to be reliable and beneficial for the evaluation of the performance of this TEG and as a valuable tool to identify room for improvement.

## 6. Conclusion

Received: May 30, 2022

Revised: June 23, 2022

Published online:

In this article, we present a fully Mg<sub>2</sub>(Si,Sn)-based TEG, with the first reported conversion efficiency measurement for such a module. The reliability of the measurement is assessed by comparing it to constant property modeling calculations, which give a satisfyingly good match (<2% deviation for current at maximum power, <3% difference for maximum power output, deviation within measurement uncertainty range for heat flow and efficiency). We report a maximum power output of 0.55 W (0.9 W cm<sup>-2</sup> considering TE area) and a maximum efficiency of 3.6%, which are well within the range of the reported silicide-based modules. The measured efficiency is likely underestimated due to radiative thermal bypass and the real value could actually reach 4%.

The cycling behavior of several module parameters as well as the deviation between measured and calculated inner electrical resistance suggests crack formation in the TE legs during thermal cycling related to TEG measurement. Room for improvement of module performance is identified and suggestions for next designs are given. The predicted maximum power output for reasonable inner resistance is 1.2 W cm<sup>-2</sup> and the predicted maximum efficiency is 5.3%, which is significantly higher than currently reported experimental values.

## Supporting Information

Supporting Information is available from the Wiley Online Library or from the author.

## Acknowledgements

The authors would like to gratefully acknowledge the endorsement for the DLR executive Board Members for Space Research and Technology, as well as financial support from the Young Research Group Leader Program. The authors would also like to acknowledge Przemyslaw Blaszkewitz for his help with the thermoelectric measurements, as well as Adina Frank for her assistance with the PVD coatings. J.C. and P.P. would like to thank the DAAD fellowship programs no. 57424731 and no. 247/2017, respectively. J.D.B. acknowledges support by the Deutsche Forschungsgemeinschaft (DFG, German Research Foundation), project number 396709363. P.Z. gratefully acknowledges financial support for the project "Thermoelectric Standardization for High Temperatures" (TEST-HT, grant number 03VP04401), granted by the German Federal Ministry of Education and Research.

Open Access funding enabled and organized by Projekt DEAL.

## Conflict of Interest

The authors declare no conflict of interest.

## Data Availability Statement

The data that support the findings of this study are available from the corresponding author upon reasonable request.

## Keywords

constant property modelling, conversion efficiency measurement, CPM, heat flow, power generation, TEG, thermoelectric generator, thermoelectrics

- [1] S. Twaha, J. Zhu, Y. Yan, B. Li, *Renewable Sustainable Energy Rev.* **2016**, *65*, 698.
- [2] S. Karellas, A.-D. Leontaritis, G. Panousis, E. Bellos, E. Kakaras, *Energy* **2013**, *58*, 147.
- [3] N. Jaziri, A. Boughamoura, J. Müller, B. Mezghani, F. Tounsi, M. Ismail, *Energy Rep.* **2020**, *6*, 264.
- [4] D. G. Ebling, A. Krumm, B. Pfeiffelmann, J. Gottschald, J. Bruchmann, A. C. Benim, M. Adam, R. Labs, R. R. Herberth, A. Stunz, *J. Electron. Mater.* **2016**, *45* 3433.
- [5] K. Li, G. Garrison, Y. Zhu, M. Moore, C. Liu, J. Hepper, L. Bandt, R. Horne, S. Petty, *J. Power Sources* **2021**, *485*, 229266.
- [6] L. K. Allison, T. L. Andrew, *Adv. Mater. Technol.* **2019**, *4* 1800615.
- [7] H. M. Elmoughni, A. K. Menon, R. M. W. Wolfe, S. K. Yee, *Adv. Mater. Technol.* **2019**, *4*, 1800708.
- [8] M. N. Hasan, M. Nafea, N. Nayan, M. S. Mohamed, *Adv. Mater. Technol.* **2022**, *7*, 2101203.
- [9] P. Gorai, V. Stevanović, E. S. Toberer, *Nat. Rev. Mater.* **2017**, *2* 17053.
- [10] B. B. Iversen, *Nat. Mater.* **2021**, *20* 1309.
- [11] G. J. Snyder, E. S. Toberer, *Materials for Sustainable Energy: A Collection of Peer-Reviewed Research and Review Articles from Nature Publishing Group*, World Scientific, London, UK **2011**, pp. 101–110.
- [12] A. Sankhla, A. Patil, H. Kamila, M. Yasseri, N. Farahi, E. Mueller, J. de Boor, *ACS Appl. Energy Mater.* **2018**, *1* 531.
- [13] H. Kamila, A. Sankhla, M. Yasseri, N.P. Hoang, N. Farahi, E. Mueller, J. de Boor, *Mater. Today: Proc.* **2019**, *8*, 546.
- [14] V. Trivedi, M. Battabyal, P. Balasubramanian, G. M. Muralikrishna, P. K. Jain, R. Gopalan, *Sustainable Energy Fuels* **2018**, *2* 2687.
- [15] S. Muthiah, R. C. Singh, B. D. Pathak, P. K. Avasthi, R. Kumar, A. Kumar, A. K. Srivastava, A. Dhar, *Nanoscale* **2018**, *10* 1970.
- [16] A. Ostovari Moghaddam, A. Shokuhfar, Y. Zhang, T. Zhang, D. Cadavid, J. Arbiol, A. Cabot, *Adv. Mater. Interfaces* **2019**, *6* 1900467.
- [17] P. Jood, J. P. Male, S. Anand, Y. Matsushita, Y. Takagiwa, M. G. Kanatzidis, G. J. Snyder, M. Ohta, *J. Am. Chem. Soc.* **2020**, *142* 15464.
- [18] K.-M. Song, D.-K. Shin, K.-W. Jang, S.-M. Choi, S. Lee, W.-S. Seo, I.-H. Kim, *J. Electron. Mater.* **2017**, *46* 2634.
- [19] R. He, G. Schierning, K. Nielsch, *Adv. Mater. Technol.* **2018**, *3* 1700256.
- [20] H. Hachiuma, K. Fukuda, in *Proc. of the Fifth European Conf. on Thermoelectrics*, Odessa, Ukraine, September 10–12 **2007**.
- [21] G. Schierning, *Nat. Energy* **2018**, *3* 92.
- [22] J. Yu, Y. Xing, C. Hu, Z. Huang, Q. Qiu, C. Wang, K. Xia, Z. Wang, S. Bai, X. Zhao, L. Chen, T. Zhu, *Adv. Mater.* **2020**, *10* 2000888.
- [23] J.-M. Oh, C. C. Venters, C. Di, A. M. Pinto, L. Wan, I. Younis, Z. Cai, C. Arai, B. R. So, J. Duan, G. Dreyfuss, *Nat. Commun.* **2020**, *11* 1.
- [24] P. Jood, M. Ohta, A. Yamamoto, M. G. Kanatzidis, *Joule* **2018**, *2* 1339.
- [25] C. Bode, J. Friedrichs, R. Somdalen, J. Köhler, K. Büchter, C. Falter, U. Kling, P. Ziolkowski, K. Zabrocki, E. Müller, D. Kožulović, *Proceedings of the ASME 2016 International Mechanical Engineering Congress and Exposition. Volume 1: Advances in Aerospace Technology*, ASME, Phoenix, Arizona, USA, November 11–17 **2016**, V001T03A041, <https://doi.org/10.1115/IMECE2016-66650>.
- [26] N. Farahi, C. Stiewe, D. Y. N. Truong, J. de Boor, E. Müller, *RSC Adv.* **2019**, *9* 23021.

- [27] A. Bali, R. Chetty, A. Sharma, G. Rogl, P. Heinrich, S. Suwas, D. K. Misra, P. Rogl, E. Bauer, R. C. Mallik, *J. Appl. Phys.* **2016**, 120 175101.
- [28] J. de Boor, T. Dasgupta, U. Saparamadu, E. Müller, Z. F. Ren, *Mater. Today Energy* **2017**, 4, 105.
- [29] H. S. Kim, K. Kikuchi, T. Itoh, T. Iida, M. Taya, *Mater. Sci. Eng., B* **2014**, 185, 45.
- [30] P. Balasubramanian, M. Battabyal, A. Chandra Bose, R. Gopalan, *Mater. Sci. Eng., B* **2021**, 271, 115274.
- [31] J. Chu, J. Huang, R. Liu, J. Liao, X. Xia, Q. Zhang, C. Wang, M. Gu, S. Bai, X. Shi, L. Chen, *Nat. Commun.* **2020**, 11, 2723.
- [32] J. Camut, N. H. Pham, D. Y. Nhi Truong, G. Castillo-Hernandez, N. Farahi, M. Yasseri, E. Mueller, J. de Boor, *Mater. Today Energy* **2021**, 21, 100718.
- [33] J. Camut, S. Ayachi, G. Castillo-Hernández, S. Park, B. Ryu, S. Park, A. Frank, C. Stiewe, E. Müller, J. de Boor, *Materials* **2021**, 14, 6774.
- [34] G. Castillo-Hernández, E. Müller, J. de Boor, *Materials* **2022**, 15, 779.
- [35] T. Sakamoto, T. Iida, Y. Taguchi, S. Kurosaki, Y. Hayatsu, K. Nishio, Y. Kogo, Y. Takanashi, *J. Electron. Mater.* **2012**, 41 1429.
- [36] T. Nemoto, T. Iida, J. Sato, T. Sakamoto, T. Nakajima, Y. Takanashi, *J. Electron. Mater.* **2012**, 41 1312.
- [37] T. Nemoto, T. Iida, J. Sato, H. Suda, Y. Takanashi, *J. Electron. Mater.* **2014**, 43 1890.
- [38] T. Nemoto, T. Iida, J. Sato, T. Sakamoto, N. Hirayama, T. Nakajima, Y. Takanashi, *J. Electron. Mater.* **2013**, 42 2192.
- [39] T. Tohei, S. Fujiwara, T. Jinushi, Z. Ishijima, *International Symposium on Interfacial Joining and Surface Technology (IJST2013)*. **2014**. Icho Kaikan, Osaka University, Japan, November 2013.
- [40] K. R. Tarantik, J. D. König, M. Jägler, J. Heuer, J. Horzella, A. Mahlke, M. Vergez, K. Bartholomé, *Mater. Today. Proc.* **2015**, 2 588.
- [41] G. Skomedal, L. Holmgren, H. Middleton, I. S. Eremin, G. N. Isachenko, M. Jaegle, K. Tarantik, N. Vlachos, M. Manoli, T. Kyratsi, D. Berthebaud, N. Y. Dao Truong, F. Gascoin, *Energy Convers. Manage.* **2016**, 110, 13.
- [42] H. Kaibe, I. Aoyama, M. Mukoujima, T. Kanda, S. Fujimoto, T. Kurosawa, H. Ishimabushi, K. Ishida, L. Rauscher, Y. Hata, S. Sano, *ICT 2005. 24th Inter. Conf. on Thermoelectrics, 2005*, IEEE, Piscataway, NJ **2005**.
- [43] P. Gao, *Mg<sub>2</sub>(Si, Sn)-Based Thermoelectric Materials and Devices*, Michigan State University, Michigan, US **2016**, p. 128.
- [44] G. K. Goyal, T. Dasgupta, *Mater. Sci. Eng., B* **2021**, 272, 115338.
- [45] P. Ponnusamy, J. de Boor, E. Müller, *Appl. Energy* **2020**, 262, 114587.
- [46] S. Ayachi, G. Castillo Hernandez, N. H. Pham, N. Farahi, E. Müller, J. de Boor, *ACS Appl. Mater. Interfaces* **2019**, 11 40769.
- [47] N. H. Pham, N. Farahi, H. Kamila, A. Sankhla, S. Ayachi, E. Müller, J. de Boor, *Mater. Today Energy* **2019**, 11, 97.
- [48] D. Platzek, G. Karpinski, C. Stiewe, P. Ziolkowski, C. Drasar, E. Müller, *ICT 2005. 24th Inter. Conf. on Thermoelectrics*, IEEE, Piscataway, NJ **2005**.
- [49] P. Ziolkowski, G. Karpinski, T. Dasgupta, E. Müller, *Physica Status Solidi* **2013**, 210 89.
- [50] M. Gao, D. M. Rowe, in *CRC Handbook of Thermoelectrics* (Ed: D.M. Rowe), CRC press, Boca Raton **1995**.
- [51] J. de Boor, C. Gloanec, H. Kolb, R. Sottong, P. Ziolkowski, E. Müller, *J. Alloys Compd.* **2015**, 632, 348.
- [52] P. Ziolkowski, P. Blaschkewitz, E. Müller, *Measurement* **2021**, 167, 108273.
- [53] P. Ziolkowski, P. Blaschkewitz, E. Müller, *Measurement* **2021**, 177, 109247.
- [54] P. Ziolkowski, R. Chetty, P. Blaschkewitz, M. Ohta, A. Yamamoto, E. Müller, *Energy Technol.* **2020**, 8 2000557.
- [55] P. Ziolkowski, P. Blaschkewitz, B. Ryu, S. Park, E. Müller, *Materials* **2022**, 15, 1627.
- [56] B. Ryu, J. Chung, S. Park, *iScience* **2021**, 24 102934.
- [57] D. M. Rowe, in *Thermoelectrics Handbook: Macro to Nano* (Ed: D.M. Rowe), CRC press, Boca Raton **2006**.
- [58] H. J. Goldsmid, in *CRC Handbook of Thermoelectrics* (Ed: D.M. Rowe), CRC press, Boca Raton **1995**.
- [59] P. Ying, R. He, J. Mao, Q. Zhang, H. Reith, J. Sui, Z. Ren, K. Nielsch, G. Schierning, *Nat. Commun.* **2021**, 12 1121.
- [60] A. Nozariasbmarz, B. Poudel, W. Li, H. B. Kang, H. Zhu, S. Priya, *iScience* **2020**, 23 101340.
- [61] S. Mahmoudinezhad, A. Rezania, P. A. Cotfas, D. T. Cotfas, L. A. Rosendahl, *Energy* **2019**, 168, 823.
- [62] R. Funahashi, S. Urata, T. Mihara, N. Nabeshima, K. Iwasaki, *Mass and Charge Transport in Inorganic Materials III*, Trans Tech Publications Ltd, October 10 **2006**, <https://doi.org/10.4028/www.scientific.net/ast.46.158>.
- [63] R. Funahashi, S. Urata, K. Mizuno, T. Kouuchi, M. Mikami, *Appl. Phys. Lett.* **2004**, 85 1036.
- [64] P. Qiu, J. Cheng, J. Chai, X. Du, X. Xia, C. Ming, C. Zhu, J. Yang, Y.-Y. Sun, F. Xu, X. Shi, L. Chen, *Adv. Mater.* **2022**, 12 2200247.
- [65] M. Mejri, Y. Thimont, B. Malard, C. Estournès, *Scr. Mater.* **2019**, 172, 28.
- [66] Y. Gelbstein, J. Tunbridge, R. Dixon, M. J. Reece, H. Ning, R. Gilchrist, R. Summers, I. Agote, M. A. Lagos, K. Simpson, C. Rouaud, P. Feulner, S. Rivera, R. Torrecillas, M. Husband, J. Crossley, I. Robinson, *J. Electron. Mater.* **2014**, 43 1703.
- [67] P. Gao, I. Berkun, R. D. Schmidt, M. F. Luzenski, X. Lu, P. Bordon Sarac, E. D. Case, T. P. Hogan, *J. Electron. Mater.* **2014**, 43 1790.
- [68] P. Qiu, T. Mao, Z. Huang, X. Xia, J. Liao, M. T. Agne, M. Gu, Q. Zhang, D. Ren, S. Bai, Xun. Shi, G. J. Snyder, L. Chen, *Joule* **2019**, 3 1538.
- [69] Z. Bu, X. Zhang, Y. Hu, Z. Chen, S. Lin, W. Li, Y. Pei, *Energy Environ. Sci.* **2021**, 14 6506.
- [70] U. Erturun, K. Erermis, K. Mossi, *Appl. Energy* **2015**, 159, 19.
- [71] N. K. Karri, C. Mo, *J. Electron. Mater.* **2018**, 47 3127.
- [72] N. K. Karri, C. Mo, *J. Electron. Mater.* **2018**, 47 6101.